Monthly Notices
of the
ROYAL ASTRONOMICAL SOCIETY

MNRAS **461,** 190–201 (2016)
Advance Access publication 2016 June 7

doi:10.1093/mnras/stw1327

Dynamical structure of magnetized dissipative accretion flow around black holes

Biplob Sarkar★ and Santabrata Das★
Indian Institute of Technology Guwahati, Guwahati 781039, India

Accepted 2016 June 1. Received 2016 June 1; in original form 2016 March 28

ABSTRACT

We study the global structure of optically thin, advection dominated, magnetized accretion flow around black holes. We consider the magnetic field to be turbulent in nature and dominated by the toroidal component. With this, we obtain the complete set of accretion solutions for dissipative flows where bremsstrahlung process is regarded as the dominant cooling mechanism. We show that rotating magnetized accretion flow experiences virtual barrier around black hole due to centrifugal repulsion that can trigger the discontinuous transition of the flow variables in the form of shock waves. We examine the properties of the shock waves and find that the dynamics of the post-shock corona (PSC) is controlled by the flow parameters, namely viscosity, cooling rate and strength of the magnetic field, respectively. We separate the effective region of the parameter space for standing shock and observe that shock can form for wide range of flow parameters. We obtain the critical viscosity parameter that allows global accretion solutions including shocks. We estimate the energy dissipation at the PSC from where a part of the accreting matter can deflect as outflows and jets. We compare the maximum energy that could be extracted from the PSC and the observed radio luminosity values for several supermassive black hole sources and the observational implications of our present analysis are discussed.

Key words: accretion, accretion discs – black hole physics – hydrodynamics – shock waves.

1 INTRODUCTION

In the quest of the accretion process around black holes, viscosity plays an important role in a differentially rotating flow which is likely to be threaded by the magnetic fields as well. Unfortunately, the source of the viscosity in an accretion disc is not yet known conclusively. Meanwhile, Balbus & Hawley (1991, 1998) showed that viscosity seems to arise in an accretion disc as a consequence of the magnetorotational instability (MRI). In this view, the Maxwell stress is generated by MRI that efficiently transports the angular momentum of the disc and at the same time the dissipation of the magnetic energy is being utilized in disc heating (Hirose, Krolik & Stone 2006). Based on the above consideration, several attempts were made to study the self-consistent global accretion solutions around black holes (Akizuki & Fukue 2006; Machida, Nakamura & Matsumoto 2006; Begelman & Pringle 2007; Oda et al. 2007, 2010, 2012; Bu, Yuan & Xie 2009; Samadi, Abbassi & Khajavi 2014). In these approaches, the description of the magnetic fields are considered to be toroidal in nature because the motion of the accreting material inside the disc is primarily governed by the differential rotation and therefore, the description of the magnetic field is expected to be dominated by the toroidal component of the magnetic fields. The work of Oda et al. (2010) demonstrates the implication of the magnetically supported disc where it was shown that the model has the potential to describe the bright/hard state observed during the bright/slow transition of galactic black hole candidates. Observational signature of such state transition was reported by Gierliński & Newton (2006).

In the conventional theory of the advective accretion disc around black holes, subsonic inflowing matter starts its journey towards black hole from the outer edge of the disc at large distance and in order to satisfy the inner boundary conditions, flow must change its sonic state to become super-sonic before crossing the horizon. In the vicinity of the black hole, rotating flow experiences centrifugal barrier against gravity that eventually triggers the discontinuous transition of the flow variables in the form of shock waves when possible. According to the second law of thermodynamics, accretion solutions containing shock waves are preferred as they possess high entropy content (Becker & Kazanas 2001). Presence of shock waves in an accretion disc around black hole has been confirmed both theoretically (Fukue 1987; Chakrabarti 1989, 1996; Lu, Gu & Yuan 1999; Das, Chattopadhyay & Chakrabarti 2001b; Chakrabarti & Das 2004) as well as numerically (Molteni, Lanzafame & Chakrabarti 1994; Molteni, Ryu & Chakrabarti 1996; Das et al. 2014; Okuda 2014; Okuda & Das 2015). Due to shock compression, the post-shock

*E-mail: biplob@iitg.ernet.in (BS); sbdas@iitg.ernet.in (SD)

matter, equivalently post-shock corona (PSC), becomes hot and dense compared to the pre-shock matter and eventually PSC behaves like an effective boundary layer of the black hole. Since PSC is composed with the swarm of hot electrons, soft-photons from the cold pre-shock matter are inverse Comptonized after intercepted at the PSC and produces the spectral features of the black holes (Chakrabarti & Titarchuk 1995). In addition, PSC deflects a part of the accreting matter to produce bipolar jets and outflows due to the excess thermal gradient force present across the shock (Chakrabarti 1999; Das et al. 2001a; Chattopadhyay & Das 2007; Das & Chattopadhyay 2008; Aktar, Das & Nandi 2015). When PSC modulates, quasi-periodic oscillation of hard radiations in the spectral states is observed (Chakrabarti & Manickam 2000; Nandi et al. 2001a,b, 2012) along with the variable outflow rates (Das et al. 2001a).

Although the shocked accretion solutions seems to have potential to describe the spectral and timing properties as well as outflow rates, no efforts are given to examine the properties of the magnetically supported accretion flow that harbours shock waves. Being motivated with this, in the present paper, we model the optically thin magnetized accretion flow around a Schwarzschild black hole. The characteristic of the magnetic pressure is assumed to be same as the gas pressure and their combined effects support the vertical structure of the disc against gravity. Following the conventional α-viscosity prescription of Shakura & Sunyaev (1973), it is evident that the angular momentum transport in the disc equatorial plane would also be enhanced as the magnetic pressure contributes to the total pressure. Towards this, we consider a set of steady state hydrodynamical equations describing the dissipative accretion flow in a disc. For simplicity, the space–time geometry around a Schwarzschild black hole is approximated by adopting the pseudo-Newtonian potential (Paczyński & Wiita 1980). We further consider that the heating of the flow is governed by the magnetic energy dissipation process and the cooling of the flow is dominated by the Comptonization of the bremsstrahlung radiation, respectively. With this, we self-consistently calculate the global accretion solution including shock waves and investigate the shock properties in terms of the flow parameters. We find that shocked accretion solution exists for a wide range of flow parameters. We also computed the critical value of viscosity parameter $\alpha_B^{\rm cri}$ for which standing shock forms in a magnetized flow. Indeed, $\alpha_B^{\rm cri}$ greatly depends on the inflow parameters. Note that $\alpha_B^{\rm cri}$ tends to $\alpha_\Pi^{\rm cri}(\sim 0.3)$ as estimated by Chakrabarti & Das (2004) for gas pressure dominated flow. This is quite obvious because in the adopted viscosity prescription, magnetic pressure contributes to the total pressure and hence, a lower value of α_B is sufficient to transport the required angular momentum for shock transition. This essentially establishes the fact that the shocks under consideration are centrifugally driven. Furthermore, we consider the shock to be dissipative in nature and compute the maximum available energy dissipated at the shock. Employing this result, we then calculate the loss of kinetic power from the disc ($L_{\rm shock}^{\rm max}$) which could be utilized to power the jets as they are likely to be launched from the PSC (Chakrabarti 1999; Das et al. 2001a; Das & Chattopadhyay 2008; Aktar et al. 2015). The above analysis apparently provides an estimate which we compare with the jet kinetic power available from observation for six sources and close agreements are seen.

The plan of the paper is as follows. In the next section, we describe the assumptions and governing equations for our model. In Section 3, we present the global accretion solutions with and without shock, shock properties, and shock parameter space. In Section 4, we apply our formalism to calculate the shock luminosity considering several astrophysical sources. In section 5, we present concluding remarks.

2 GOVERNING EQUATIONS

We begin with the consideration that the magnetic fields inside the accretion disc are turbulent in nature and the azimuthal component of the magnetic fields dominates over other component. Numerical study of global MHD accretion flow around black holes in the quasi-steady state supports the above findings (Hirose et al. 2006; Machida et al. 2006). Based on the simulation work, the magnetic fields are considered as a combination of mean fields and the fluctuating fields. The mean fields are denoted as $\boldsymbol{B} = (0, \langle B_\phi \rangle, 0)$ where, $\langle\rangle$ indicates the azimuthal average and the fluctuating fields are represented by $\delta\boldsymbol{B} = (\delta B_r, \delta B_\phi, \delta B_z)$. When the fluctuating fields are averaged azimuthally, we assume that they eventually disappear. Therefore, the azimuthal component of magnetic fields dominates over the other components as they are negligible, $|\langle B_\phi \rangle + \delta B_\phi| \gg |\delta B_r|$ and $|\delta B_z|$. This essentially yields the azimuthally averaged magnetic field as $\langle \boldsymbol{B} \rangle = \langle B_\phi \rangle \hat{\phi}$ (Oda et al. 2007).

In this work, we use geometric units as $2G = M_{\rm BH} = c = 1$, where G, $M_{\rm BH}$ and c are the gravitational constant, mass of the black hole and the speed of light, respectively. In this unit system, length, time and velocity are expressed in unit of $r_g = 2GM_{\rm BH}/c^2$, $2GM_{\rm BH}/c^3$ and c, respectively. Here, we assume that the matter accretes through the equatorial plane of a Schwarzschild black hole. We use cylindrical polar coordinates (x, ϕ, z) with the black hole at the origin and the disc lies in the $z = 0$ plane. We adopt the pseudo-Newtonian potential (Paczyński & Wiita 1980) to describe the space–time geometry around the black hole and is given by

$$\Phi = -\frac{1}{2(x-1)}, \tag{1}$$

where, x is the non-dimensional radial distance.

The gas pressure inside the disc is obtained as $p_{\rm gas} = R\rho T/\mu$, where, R is the gas constant, ρ is the density, T is the temperature and μ is the mean molecular weight assumed to be 0.5 for fully ionized hydrogen. The magnetic pressure is given by, $p_{\rm mag} = \langle B_\phi^2 \rangle / 8\pi$, where, $\langle B_\phi^2 \rangle$ is the azimuthal average of the square of the toroidal component of the magnetic field. We denote the total pressure in the disc by $P = p_{\rm gas} + p_{\rm mag}$. We define plasma β as the ratio of gas pressure ($p_{\rm gas}$) to the magnetic pressure ($p_{\rm mag}$) inside the disc which yields $P = p_{\rm gas}(1 + 1/\beta)$. The adiabatic sound speed is defined as $a = \sqrt{\gamma P/\rho}$, where γ is the adiabatic index assumed to be constant throughout the flow. We adopt the canonical value of $\gamma = 1.5$ in the subsequent analysis. We consider the disc to be axisymmetric, steady and thin. Following this, we compute the half thickness of the disc (h) considering the flow is in hydrostatic equilibrium in the transverse direction and is given by

$$h = \sqrt{\frac{2}{\gamma}} a x^{1/2} (x-1). \tag{2}$$

With this, we have the following governing equations that describe the accreting matter in the steady state as:

(a) Radial momentum equation:

$$v\frac{{\rm d}v}{{\rm d}x} + \frac{1}{\rho}\frac{{\rm d}P}{{\rm d}x} - \frac{\lambda^2(x)}{x^3} + \frac{1}{2(x-1)^2} + \frac{\langle B_\phi^2 \rangle}{4\pi x \rho} = 0. \tag{3}$$

where, v is the radial velocity and $\lambda(x)$ is the specific angular momentum at radial coordinate x. The last term on the left-hand side represents the magnetic tension force.

(b) Mass Conservation:

$$\dot{M} = 2\pi x \Sigma v, \tag{4}$$

where, $\dot{M}$ is the rate at which the black hole is continuously accreting matter and remain constant throughout the flow. Σ represent the vertically integrated density of flow (Matsumoto et al. 1984).

(c) Azimuthal momentum equation:

$$v\frac{\mathrm{d}\lambda(x)}{\mathrm{d}x}+\frac{1}{\Sigma x}\frac{\mathrm{d}}{\mathrm{d}x}(x^2T_{x\phi})=0, \tag{5}$$

where, we consider that the vertically integrated total stress is dominated by the $x\phi$ component of the Maxwell stress $T_{x\phi}$. Following Machida et al. (2006), we estimate $T_{x\phi}$ for an advective flow with significant radial velocity (Chakrabarti & Das 2004) as

$$T_{x\phi}=\frac{\langle B_x B_\phi\rangle}{4\pi}h=-\alpha_B(W+\Sigma v^2), \tag{6}$$

where, α_B is the proportionality constant and W is the vertically integrated pressure (Matsumoto et al. 1984). In this study, we treat α_B as a parameter based on the seminal work of Shakura & Sunyaev (1973). For a Keplerian flow where the radial velocity is unimportant, equation (6) subsequently reduces to the original prescription of 'α-model' (Shakura & Sunyaev 1973).

(d) The entropy generation equation:

$$\Sigma vT\frac{\mathrm{d}s}{\mathrm{d}x}=\frac{hv}{\gamma-1}\left(\frac{\mathrm{d}P}{\mathrm{d}x}-\frac{\gamma P}{\rho}\frac{\mathrm{d}\rho}{\mathrm{d}x}\right)=Q^--Q^+, \tag{7}$$

where, we consider $\beta>1$ inside the flow. Subsequently, we assume $\beta/(\beta+1)\sim 1$ and neglect term with $1/(\beta+1)^2$ for a modest value of β. Here, s and T represent the specific entropy and the local temperature of the flow, respectively. In the right-hand side, Q^+ and Q^- denote the vertically integrated heating and cooling rates. The flow is heated due to the thermalization of magnetic energy through the magnetic reconnection mechanism (Hirose et al. 2006; Machida et al. 2006) and therefore, expressed as

$$Q^+=\frac{\langle B_x B_\phi\rangle}{4\pi}xh\frac{\mathrm{d}\Omega}{\mathrm{d}x}=-\alpha_B(W+\Sigma v^2)x\frac{\mathrm{d}\Omega}{\mathrm{d}x}, \tag{8}$$

where, Ω denotes the angular velocity of the flow.

The cooling of the flow could be due to the various physical processes, namely bremsstrahlung, synchrotron, Comptonization etc. For simplicity, in this work, we assume the Comptonization of the bremsstrahlung radiation where the intensity of the bremsstrahlung photons are enhanced by a factor ξ. Evidently, $1<\xi<\sim$ few $\times$ 100, depending on the availability of soft photons (Chakrabarti & Titarchuk 1995; Das & Chakrabarti 2004). In a way, ξ is treated as dimensionless parameter in the form of cooling efficiency factor to represent net cooling. When $\xi=0$, flow becomes heating dominated as it cools inefficiently. In this view, the cooling rate of the flow is given by (Shapiro & Teukolsky 1983),

$$Q^-=\xi\times\frac{C\rho h}{vx^{3/2}(x-1)}\left[\frac{\beta}{1+\beta}\right]^{1/2}, \tag{9}$$

with

$$C=1.974\times10^{-10}\left(\frac{m_\mathrm{e}}{m_\mathrm{p}}\right)^{1/4}\left[\frac{\mu m_\mathrm{p}}{2k_\mathrm{B}}\right]^{1/2}\frac{\dot{m}}{4\pi I_n m_\mathrm{p}^2}\frac{1}{2GcM_\odot},$$

where, m_p is the mass of the ion, m_e is the mass of the electron, k_B is the Boltzmann constant, $I_n=(2^n n!)^2/(2n+1)!$ and $n=1/(\gamma-1)$. In this analysis, we ignore any coupling between the ions and electrons and estimate the electron temperature using the relation $T_\mathrm{e}=\sqrt{m_\mathrm{e}/m_\mathrm{p}}T_\mathrm{p}$ (Chattopadhyay & Chakrabarti 2002). Furthermore, here $\dot{m}$ represents the accretion rate measured in units of Eddington rate and we consider $\dot{m}=0.05$ all throughout the paper until otherwise stated.

(e) Radial advection of the toroidal magnetic flux:
In order to describe the advection rate of the toroidal magnetic flux we consider the induction equation which is given by

$$\frac{\partial\langle B_\phi\rangle\hat{\phi}}{\partial t}=\nabla\times\left(\boldsymbol{v}\times\langle B_\phi\rangle\hat{\phi}-\frac{4\pi}{c}\eta\boldsymbol{j}\right), \tag{10}$$

where, $\boldsymbol{v}$ is the velocity and $\boldsymbol{j}=c\left(\nabla\times\langle B_\phi\rangle\hat{\phi}\right)/4\pi$ is the current density. Here, equation (10) is azimuthally averaged and the dynamo and magnetic-diffusion terms are neglected. In the steady state, the resulting equation is then vertically averaged considering the fact that the averaged toroidal magnetic fields vanish at the surface of the disc. This yields the advection rate of the toroidal magnetic flux as (Oda et al. 2007)

$$\dot{\Phi}=-\sqrt{4\pi}vhB_0(x), \tag{11}$$

where

$$\begin{aligned}B_0(x)&=\langle B_\phi\rangle(x;z=0)\\&=2^{5/4}\pi^{1/4}(RT/\mu)^{1/2}\Sigma^{1/2}h^{-1/2}\beta^{-1/2}\end{aligned}$$

is the azimuthally averaged toroidal magnetic field lies in the disc equatorial plane. According to equation (10), $\dot{\Phi}$ is expected to vary with radial coordinate of the accretion disc due to the presence of the dynamo term and the magnetic-diffusion term. Meanwhile, Machida et al. (2006) numerically showed out that $\dot{\Phi}\propto x^{-1}$, when the disc is in quasi-steady state. Following this result, we adopt a parametric relation between $\dot{\Phi}$ and x which is given by (Oda et al. 2007)

$$\dot{\Phi}\left(x;\zeta,\dot{M}\right)\equiv\dot{\Phi}_\mathrm{edge}(\dot{M})\left(\frac{x}{x_\mathrm{edge}}\right)^{-\zeta}, \tag{12}$$

where, $\dot{\Phi}_\mathrm{edge}$ denotes the advection rate of the toroidal magnetic flux at the outer edge of the disc (x_edge). Note that the conservation of the magnetic flux is restored when $\zeta=0$. However, for $\zeta>0$, the magnetic flux increases as the accreting matter proceeds towards the black hole horizon. In this work, we consider ζ to remain constant all throughout and adopt $\zeta=1$ for representation, until otherwise stated.

2.1 Sonic point analysis

In order to study the dynamical structure of the accretion flow, one needs to obtain the global accretion solution where infalling matter from the outer edge of the disc can smoothly accrete inwards before entering in to the black hole. In addition, it is necessary for the accretion solution to become transonic in nature in order to satisfy the inner boundary conditions imposed by the black hole event horizon. Based on the above insight, we visualize the general nature of the sonic points by solving equations (3)– (7) and equations (11)–(12) simultaneously (Das 2007) which is expressed as

$$\frac{\mathrm{d}v}{\mathrm{d}x}=\frac{N}{D}, \tag{13}$$

where, the numerator (N) is given by

$$\begin{aligned}N=&\frac{C}{vx^{3/2}(x-1)}\frac{\beta^{1/2}}{(1+\beta)^{1/2}}+\frac{2\alpha_B^2I_n(a^2g+\gamma v^2)^2}{\gamma^2xv}\\&+\frac{2\alpha_B^2gI_na^2(5x-3)(a^2g+\gamma v^2)}{\gamma^2vx(x-1)}\\&-\left[\frac{\lambda^2}{x^3}-\frac{1}{2(x-1)^2}\right]\left[\frac{(\gamma+1)v}{(\gamma-1)}-\frac{4\alpha_B^2gI_n(a^2g+\gamma v^2)}{\gamma v}\right]\end{aligned}$$

$$-\frac{va^2(5x-3)}{x(\gamma-1)(x-1)}-\frac{4\lambda\alpha_B I_n(a^2g+\gamma v^2)}{\gamma x^2}$$
$$-\frac{8\alpha_B^2 I_n a^2\, g(a^2g+\gamma v^2)}{\gamma^2 v(1+\beta)x}+\frac{2(\gamma+1)a^2 v}{\gamma(\gamma-1)(1+\beta)x} \quad (13a)$$

and the denominator D is

$$D=\frac{2a^2}{(\gamma-1)}-\frac{(\gamma+1)v^2}{(\gamma-1)}$$
$$+\frac{2\alpha_B^2 I_n(a^2g+\gamma v^2)}{\gamma}\left[(2g-1)-\frac{a^2 g}{\gamma v^2}\right]. \quad (13b)$$

Here, we write $g = I_{n+1}/I_n$.

The gradient of sound speed is calculated as

$$\frac{\mathrm{d}a}{\mathrm{d}x}=\left(\frac{a}{v}-\frac{\gamma v}{a}\right)\frac{\mathrm{d}v}{\mathrm{d}x}+\frac{\gamma}{a}\left[\frac{\lambda^2}{x^3}-\frac{1}{2(x-1)^2}\right]$$
$$+\frac{(5x-3)a}{2x(x-1)}-\frac{2a}{(1+\beta)x}. \quad (14)$$

The gradient of angular momentum is obtained as

$$\frac{\mathrm{d}\lambda}{\mathrm{d}x}=-\frac{\alpha_B x(a^2g-\gamma v^2)}{\gamma v^2}\frac{\mathrm{d}v}{\mathrm{d}x}+\frac{2\alpha_B a x g}{\gamma v}\frac{\mathrm{d}a}{\mathrm{d}x}+\frac{\alpha_B(a^2g+\gamma v^2)}{\gamma v}. \quad (15)$$

The gradient of plasma β is given by

$$\frac{\mathrm{d}\beta}{\mathrm{d}x}=\frac{(1+\beta)}{v}\frac{\mathrm{d}v}{\mathrm{d}x}+\frac{3(1+\beta)}{a}\frac{\mathrm{d}a}{\mathrm{d}x}+\frac{1+\beta}{x-1}+\frac{(1+\beta)(4\zeta-1)}{2x}. \quad (16)$$

Matter starts accreting towards the black hole from the outer edge of the disc with almost negligible velocity and subsequently crosses the black hole horizon with velocity equal to the speed of light. This suggests that the accretion flow trajectory must be smooth along the streamline and therefore, the radial velocity gradient would be necessarily real and finite always. However, equation (13b) indicates that there may be some points between the outer edge of the disc and the horizon, where the denominator (D) vanishes. To maintain the flow to be smooth everywhere along the streamline, the point where D tends to zero, N must also vanish there. The point where both N and D vanish simultaneously is a special point and called as sonic point (x_c). Thus, we have $N = D = 0$ at the sonic point. Setting $D = 0$, we obtain the expression of the Mach number ($M = v/a$) at the sonic point which is calculated as

$$M_c=\sqrt{\frac{-m_b-\sqrt{m_b^2-4m_a m_c}}{2m_a}}, \quad (17)$$

where

$$m_a = 2\alpha_B^2 I_n\gamma(\gamma-1)(2g-1)-\gamma(\gamma+1)$$
$$m_b = 2\gamma+4\alpha_B^2 I_n g(g-1)(\gamma-1)$$
$$m_c = -(2\alpha_B^2 I_n g^2(\gamma-1))/\gamma.$$

Setting $N = 0$, we obtain the algebraic equation of the sound speed at the sonic point and is given by,

$$\mathcal{A}_c a^4(x_c)+\mathcal{B}_c a^3(x_c)+\mathcal{C}_c a^2(x_c)+\mathcal{D}_c=0, \quad (18)$$

where

$$\mathcal{A}_c=\frac{2\alpha_B^2 I_n\left(g+\gamma M_c^2\right)^2}{\gamma^2 x_c}+\frac{2\alpha_B^2 I_n g(5x_c-3)\left(g+\gamma M_c^2\right)}{\gamma^2 x_c(x_c-1)}$$
$$-\frac{M_c^2(5x_c-3)}{x_c(\gamma-1)(x_c-1)}-\frac{8\alpha_B^2 I_n g\left(g+\gamma M_c^2\right)}{\gamma^2(1+\beta_c)x_c}$$
$$+\frac{2(\gamma+1)M_c^2}{\gamma(\gamma-1)(1+\beta_c)x_c},$$

$$\mathcal{B}_c=-\frac{4\lambda_c\alpha_B I_n M_c(g+\gamma M_c^2)}{\gamma x_c^2},$$

$$\mathcal{C}_c=-\left[\frac{\lambda_c^2}{x_c^3}-\frac{1}{2(x_c-1)^2}\right]$$
$$\times\left[\frac{(\gamma+1)M_c^2}{(\gamma-1)}-\frac{4\alpha_B^2 g I_n(g+\gamma M_c^2)}{\gamma}\right],$$

and

$$\mathcal{D}_c=\frac{C}{x_c^{3/2}(x_c-1)}\sqrt{\frac{\beta_c}{1+\beta_c}}$$

Here, the subscript 'c' denotes the flow variables at the sonic point.

We solve equation (18) to calculate the sound speed at the sonic point knowing the input parameters of the flow and subsequently, we obtain the radial velocity at the sonic point from equation (17). Following this, it is straight forward to study the properties of the sonic points and its classification through the extensive investigation of equation (13). At the sonic point, $\mathrm{d}v/\mathrm{d}x$ generally owns two distinct values corresponding to accretion and wind solutions. When both the derivatives are real and of opposite sign, the sonic point is considered to be a matter of special interest as the global transonic solutions only pass through it and such a point is called as saddle type sonic point (Chakrabarti & Das 2004). In this work, our main focus is to examine the dynamical structure of accretion flow and its various properties and therefore, the wind solutions are left aside.

3 GLOBAL ACCRETION SOLUTION

In order to obtain a global accretion solution, we solve equations (13)– (16) simultaneously knowing the boundary values of angular momentum (λ), plasma β, cooling efficiency factor (ξ) and α_B at a given radial distance (x). Since the black hole solutions are necessarily transonic, flow must pass through the sonic point and therefore, it is convenient to supply the boundary values of the flow at the sonic point. With this, we integrate equations (13)– (16) from the sonic point once inward up to the black hole horizon and then outward up to a large distance (equivalently 'disc outer edge') and finally join them to obtain a complete global transonic accretion solution. Depending on the input parameters, flow may possess single or multiple sonic points (Das et al. 2001b). When the sonic points form close to the horizon, they are called as inner sonic points ($x_{\rm in}$) and when they form far away from the horizon, they are called as outer sonic points ($x_{\rm out}$), respectively.

3.1 Shock free global accretion solution

In Fig. 1, we present the examples of accretion solutions where the variation of Mach number ($M = v/a$) is plotted as function of logarithmic radial distance (x). The solid curve marked 'a' represents a global accretion solution passing through the inner sonic point $x_{\rm in} = 2.9740$ with angular momentum $\lambda_{\rm in} = 1.4850$, $\beta_{\rm in} = 27.778$, $\alpha_B = 0.01$ and $\xi = 10$, respectively, and connects the BH

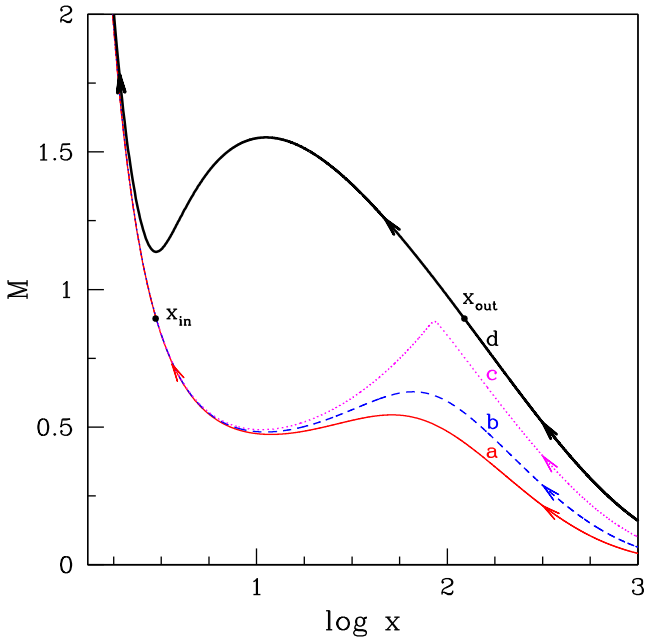

Figure 1. Radial dependence of Mach number ($M = v/a$) of the accreting matter for different values of angular momentum ($\lambda_{\rm edge}$) at the outer edge $x_{\rm edge} = 1000$ where $\beta_{\rm edge} = 1400$, $\alpha_B = 0.01$ and $\xi = 10$. Thin solid and dashed curves represent the results for $\lambda_{\rm edge} = 5.9459$ and 4.1443, respectively. For the same set of outer edge parameters, the minimum angular momentum that provides the accretion solution passing through the inner sonic is identified as $\lambda^{\rm min}_{\rm edge} = 3.0619$ (dotted curve). When $\lambda_{\rm edge} < \lambda^{\rm min}_{\rm edge}$, accretion solutions pass through the outer sonic point only (thick solid curve) where $\lambda_{\rm edge} = 2.4021$. In the figure, the locations of the inner sonic point ($x_{\rm in}$) and outer sonic point ($x_{\rm out}$) are marked and arrows indicate the direction of the flow towards the black hole. See text for details.

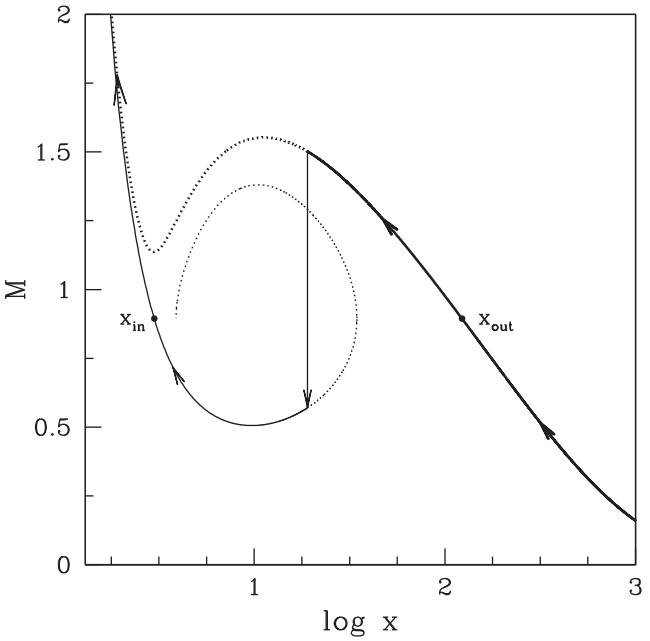

Figure 2. A complete global accretion solution containing shock ($x_s = 19.03$) is depicted along with outer ($x_{\rm out}$) and inner ($x_{\rm in}$) sonic points. Inflow parameters at the outer edge are same as case (d) of Fig. 1. See text for details.

horizon with the outer edge of the disc $x_{\rm edge}$ where we note the values of the flow variables $\lambda_{\rm edge} = 5.9459$, $\beta_{\rm edge} = 1400$, $v_{\rm edge} = 0.001\,32$, $a_{\rm edge} = 0.032\,05$ at $x_{\rm edge} = 1000$. Alternatively, one can obtain the same solution when the integration is carried out towards the black hole starting from the outer edge of the disc ($x_{\rm edge}$) with the noted boundary values. Hence, the above result essentially represents the solution of an accretion flow that starts its journey from $x_{\rm edge} = 1000$ and crosses the inner sonic point at $x_{\rm in} = 2.9740$ before entering into the black hole. The arrow indicates the direction of the flow. Now, we decrease $\lambda_{\rm edge} = 4.1443$ keeping all the other values of the flow variables same at $x_{\rm edge} = 1000$ and obtain the global transonic solution by suitably adjusting the values of $v_{\rm edge} = 0.001\,89$ and $a_{\rm edge} = 0.029\,62$. The solution is marked as 'b'. Here, the values of $v_{\rm edge}$ and $a_{\rm edge}$ is required additionally to start the integration as the sonic point is not known a priori. Following this approach, we identify the minimum value of angular momentum at the outer edge $\lambda^{\rm min}_{\rm edge} = 3.0619$, below this value accretion solution fails to pass through the inner sonic point. Accretion solution corresponding to the minimum $\lambda^{\rm min}_{\rm edge}$ is indicated by the dotted curve and marked as 'c'. The results namely 'a–c' represent solutions similar to the solution of advection dominated accretion flow around black holes (Narayan, Kato & Honma 1997; Oda et al. 2007), although another important class of solutions still remains unexplored which we present in this work. As $\lambda^{\rm min}_{\rm edge}$ is decreased further, such as 2.4021, accretion solution changes its character and passes through the outer sonic point ($x_{\rm out} = 122.9$) instead of inner sonic point ($x_{\rm in}$) with angular momentum ($\lambda_{\rm out} = 1.5631$), $\beta_{\rm out} = 431.8$ which is indicated by the thick solid line marked as 'd'. In the frame work of magnetically supported accretion disc, accretion solution passing through the outer sonic points was not studied so far. Solutions particularly of this kind are potentially interesting as they may possess centrifugally supported shock waves. The presence of shock wave in an accretion flow has profound implications as it satisfactorily delineates the spectral and temporal behaviour of numerous black hole sources (Chakrabarti 1989, 1990, 1996; Molteni et al. 1994, 1996; Lu et al. 1999; Becker & Kazanas 2001; Das et al. 2001b, 2014; Chakrabarti & Das 2004; Gu & Lu 2004; Le & Becker 2004, 2005; Becker, Das & Le 2008; Das, Becker & Le 2009; Nagakura & Yamada 2009; Nandi et al. 2012; Okuda 2014; Aktar et al. 2015; Iyer, Nandi & Mandal 2015; Okuda & Das 2015; Suková & Janiuk 2015). Thus, in this work we intend to study the properties of magnetically supported accretion solutions that possesses shock waves.

3.2 Shock induced global accretion solution

In Fig. 2, we present a global accretion solution that contains shock wave where the flow crosses the sonic region multiple times. Here, we consider inflowing matter that starts accreting towards the black hole subsonically with the boundary values at the outer edge same as the case 'd' of Fig. 1 and becomes supersonic after crossing the outer sonic point at $x_{\rm out} = 122.9$. As the rotating matter proceeds further, it experiences virtual barrier due to centrifugal repulsion and starts piling up there. The process continues and at some point, the flow eventually encounters discontinuous transition of flow variables in the form of shock when shock conditions are satisfied. This is because the shock solutions are thermodynamically preferred as the post-shock matter possesses high entropy content (Becker & Kazanas 2001). Following Landau & Lifshitz (1959), the conditions for shock transition in a vertically averaged flow are considered as the conservation of (a) mass flux ($\dot{M}_- = \dot{M}_+$) (b) the momentum flux ($W_- + \Sigma_- v_-^2 = W_+ + \Sigma_+ v_+^2$) (c) the energy flux, obtained integrating equation (3) ($\mathcal{E}_- = \mathcal{E}_+$) and (d) the magnetic

flux ($\dot{\Phi}_- = \dot{\Phi}_+$) across the shock. Here, the quantities having subscripts '−' and '+' are referred to the values before and after the shock. While doing so, we assume the shock to be thin and non-dissipative. In the post-shock region, flow momentarily slows down as it becomes subsonic immediately after the shock transition and the pre-shock kinetic energy is then converted in to the thermal energy. Therefore, the post-shock matter essentially becomes hot and dense. Due to gravitational attraction, subsonic post-shock matter continues to accrete towards the BH and gradually picks up its radial velocity and subsequently crosses the inner sonic point smoothly in order to satisfy the supersonic inner boundary condition before jumping in to the black hole. In the figure, we depict the variation of Mach number with the logarithmic radial distance. Thick curve denotes the accretion solution passing through the outer sonic point which in principle can enter in to the black hole directly. Interestingly, on the way towards the black hole, as the shock conditions are satisfied, flow makes discontinuous jump from the supersonic branch to the subsonic branch avoiding thick dotted part of the solution. In the figure, the joining of the supersonic pre-shock flow with the subsonic post-shock flow is indicated by the vertical arrow and the thin solid line denotes the inner part of the solution representing the post-shock flow. Here, $x_{\rm in}$ and $x_{\rm out}$ are the inner and outer sonic points, respectively. Arrows indicate the overall direction of the flow motion during accretion towards black hole.

In Fig. 3, we study the structure of a vertically averaged accretion disc corresponding to the solution depicted in Fig. 2. Here, each panel shows the variation of flow variables as function of logarithmic radial distance. In Fig. 3(a), we demonstrate the radial velocity (v) variation of the accreting flow where the shock transition is observed at ($x_s = 19.03$) indicated by the vertical arrow. In Fig. 3(b), we show the density profile of the flow where the catastrophic jump of density at the shock location is observed. This

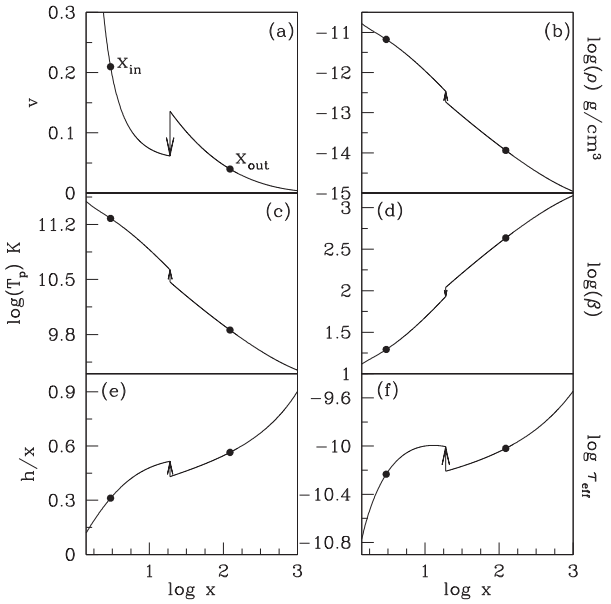

Figure 3. Variation of (a) radial velocity, (b) density in g cm^{-3}, (c) temperature (d) ratio of gas pressure to magnetic pressure, (e) disc scaleheight (h/x) and (f) effective optical depth as function of radial coordinate around a Schwarzschild black hole. All the flow variables correspond to the solution depicted in Fig. 2. Filled circles represent the sonic points where the closer one is the inner sonic point and the furthest one is the outer sonic point. Vertical arrows indicate the location of the shock location $x_s = 19.03$. See text for details.

happens mainly due to the reduction of radial velocity in the post-shock flow where the conservation of mass accretion is preserved across the shock. The formation of shock causes the compression of the post-shock flow that along with the enhancement of density effectively increases the temperature of the flow at the inner part of the disc which we represent in Fig. 3(c). We display the variation of plasma β in Fig. 3(d) where a noticeable reduction of β is seen at the shock location. In Fig. 3(e), we present the dependence of the vertical scaleheight (h/x) on the radial coordinate. Here, we observe that the half thickness of the disc always remain smaller than the local radial coordinate all the way from the outer edge of the disc to the horizon even in presence of shock wave. We estimate the effective optical depth as $\tau_{\rm eff} = \sqrt{\tau_{\rm es}\tau_{\rm br}}$ where, $\tau_{\rm es}$ denotes the scattering optical depth given by $\tau_{\rm es} = \kappa_{\rm es}\rho h$ and the electron scattering opacity is given by $\kappa_{\rm es} = 0.38\,{\rm cm^2 g^{-1}}$. Here, $\tau_{\rm br}$ represents the absorption effect appears due to thermal processes and is given by $\tau_{\rm br} = \left(hq_{\rm br}/4\sigma T_e^4\right)\left(2GM_{\rm BH}/c^2\right)$ where, $q_{\rm br}$ is the bremsstrahlung emissivity (Shapiro & Teukolsky 1983) and σ is the Stefan–Boltzmann constant. For the purpose of representation, here we consider $M_{\rm BH} = 10^6\,{\rm M}_\odot$. We find that the post-shock flow remain optically thin ($\tau < 1$) although the density profile is steeper there. This intuitively suggests that the possibility of escaping hard radiations from the PSC would be quite significant.

3.3 Shock dynamics and properties

Here, we examine the effect of cooling on the dynamical structure of the accretion flow that contain shock waves. In order for that we fix the outer edge of the disc at $x_{\rm edge} = 1000$ and inject matter subsonically with local angular momentum $\lambda_{\rm edge} = 1.88$, $\beta_{\rm edge} = 500$, $\mathcal{E}_{\rm edge} = 1.9133 \times 10^{-4}$ and $\alpha_B = 0.01$, respectively. First, we consider a cooling free flow ($\xi = 0$) that becomes supersonic after crossing the outer sonic point ($x_{\rm out} = 521.22$) and continues its journey towards the black hole. Meanwhile, stationary shock conditions are satisfied and accreting matter encounters a shock transition depicted in Fig. 4 where Mach number (M) of the flow is plotted as function of logarithmic radial coordinate. The solid vertical arrow indicates the location of the standing shock at $x_s = 39.27$ for flows having no cooling. Next, we introduce cooling considering the flow parameters at the outer edge same as in the cooling free case. When cooling efficiency factor $\xi = 100$ is supplied, shock forms at $x_s = 24.20$ indicated by the dotted vertical arrow. In reality, due to shock compression, the density and temperature in the post-shock flow are enhanced compared to the pre-shock flow and therefore, cooling is very much effective there that reduces the post-shock pressure significantly. This causes the shock front to move forward towards the horizon in order to maintain the pressure balance on either sides of the shock. This clearly indicates that the dynamics of the shock in a way are controlled by the resultant pressure across it. With the gradual increase of the cooling factor ξ, shock front proceeds closer to the BH horizon. Following this, we identify the extreme value of cooling factor $\xi = 190$ that provides the global accretion solution including shock waves at $x_s = 16.78$ for the same outer boundary parameters as considered in cooling free case. The shock location for $\xi = 190$ is represented by the dashed vertical line in the figure. When ξ is increased further, shocked accretion solution ceases to exist as the shock conditions are not satisfied there. Note that we obtain the shock induced global accretion solution even for very high cooling efficiency factor. This is possible because the effect of bremsstrahlung cooling in an accretion flow is normally weak as pointed out by Chattopadhyay & Chakrabarti (2000) and Das & Chakrabarti (2004).

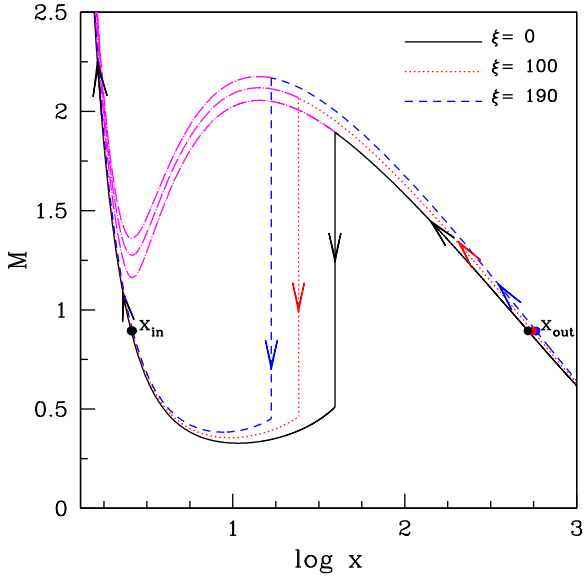

Figure 4. Plot of Mach number with logarithmic radial distance for different values of cooling factor (ξ). Accreting flows are injected from $x_{\rm edge} = 1000$ with $\lambda_{\rm edge} = 1.88$, $\mathcal{E}_{\rm edge} = 1.9133 \times 10^{-4}$, $\beta_{\rm edge} = 500$, and $\alpha_B = 0.01$. Solution obtained for cooling free case ($\xi = 0$) is denoted by the solid curve whereas dotted and dashed curves represent the solution for $\xi = 100$ and 190, respectively. The corresponding shock locations are indicated by the vertical arrow as $x_s = 39.27$ (solid), 24.20 (dotted) and 16.78 (dashed). Sonic points are marked by the filled circles.

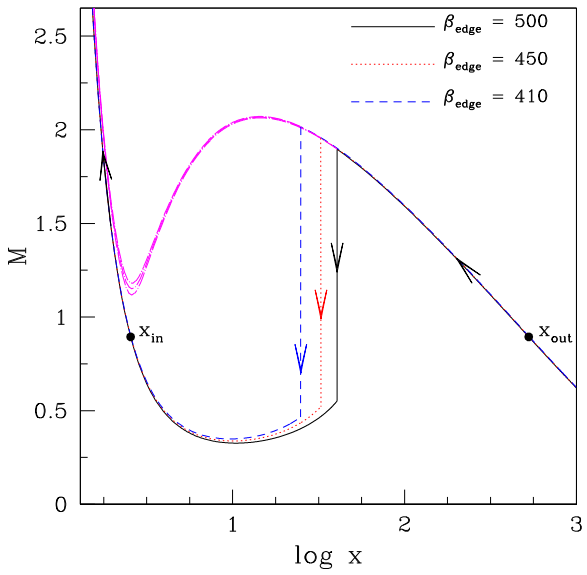

Figure 5. Plot of Mach number with logarithmic radial distance for different values of $\beta_{\rm edge}$. Accreting flows are injected from $x_{\rm edge} = 1000$ with $\lambda_{\rm edge} = 1.886$, $\mathcal{E}_{\rm edge} = 1.9133 \times 10^{-4}$, $\alpha_B = 0.01$ and $\xi = 20$. Solutions represented by the solid, dotted and dashed curves are for $\beta_{\rm edge} = 500$, 450 and 410, respectively. The corresponding shock locations are indicated by the vertical arrows as $x_s = 40.60$ (solid), 32.69 (dotted) and 24.94 (dashed). Sonic points are marked by the filled circles. See text for details.

In our subsequent analysis, we explore the response of $\beta_{\rm edge}$ on shock dynamics. While doing this, we inject matter from the outer edge at $x_{\rm edge} = 1000$ with $\lambda_{\rm edge} = 1.886$, $\mathcal{E}_{\rm edge} = 1.9133 \times 10^{-4}$, $\alpha_B = 0.01$ and $\xi = 20$, and vary $\beta_{\rm edge}$. In Fig. 5, solid, dotted and dashed curves represent the results corresponding to

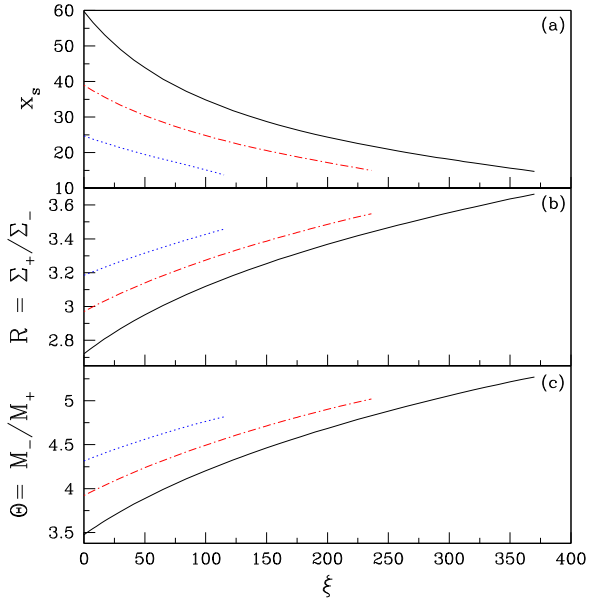

Figure 6. Variation of different flow properties such as (a) the shock location x_s, (b) shock compression ratio R, and (c) shock strength Θ as a function of ξ for flows injected from $x_{\rm edge} = 1000$ with $\alpha_B = 0.01$, $\beta_{\rm edge} = 550$ and $\mathcal{E}_{\rm edge} = 1.9133 \times 10^{-4}$ but with different $\lambda_{\rm edge}$. Solid curve corresponds to the result obtained for $\lambda_{\rm edge} = 1.890$ and the dot–dashed and dotted curves are for $\lambda_{\rm edge} = 1.873$ and 1.856, respectively. See text for details.

$\beta_{\rm edge} = 500$, 450 and 410, respectively. Here, the shock front moves inward as $\beta_{\rm edge}$ is decreased. This eventually indicates the fact that the size of the PSC decreases with the increase of the magnetic pressure inside the disc. In reality, the decrease of $\beta_{\rm edge}$ implies the increment of magnetic turbulence inside the disc. The growth of the turbulent magnetic field increases of Maxwell stress that leads to enhance the angular momentum transport outward. Hence, the centrifugal support against gravity becomes weak that pushes shock front inward. The dynamics of the shock location is eventually controlled due to the combined effect of cooling and magnetic field.

In Fig. 6, we present the comparison of shock properties as function of the cooling efficiency factor (ξ). In the upper panel (Fig. 6a), we show the variation of shock locations for different values of $\lambda_{\rm edge}$. Here, we choose the outer edge of the disc at $x_{\rm edge} = 1000$ and inject matter with $\mathcal{E}_{\rm edge} = 1.9133 \times 10^{-4}$, $\beta_{\rm edge} = 550$ and $\alpha_B = 0.01$ for all cases. The solid curve denotes the result corresponding to $\lambda_{\rm edge} = 1.890$ and the dot–dashed and dotted curves are for $\lambda_{\rm edge} = 1.873$ and 1.856, respectively. It is clear from the figure that stationary shocks in an accretion flow can be obtained for a wide range of ξ. For a given $\lambda_{\rm edge}$, the shock front is shifted towards the horizon with the increase of the cooling factor (ξ) as depicted in Fig. 4. This is because the flow loses its energy due to cooling during accretion. With this, when ξ exceeds its critical value, shock disappears as the standing shock conditions are not satisfied. This eventually provides an indication that the possibility of stationary shock transition is likely to be reduced with the increase of ξ. Evidently, the critical value of ξ largely depends on the accretion flow parameters at the outer edge. Moreover, above the critical cooling limit, the accretion flow still may contain shock waves which are oscillatory in nature and the investigation of such shock properties is beyond the scope of this paper. In addition, for a given ξ, shock recedes away from the horizon when $\lambda_{\rm edge}$ is increased. This is not surprising as the large $\lambda_{\rm edge}$ enhances the strength of the centrifugal barrier that pushes the shock front outside. This clearly indicates

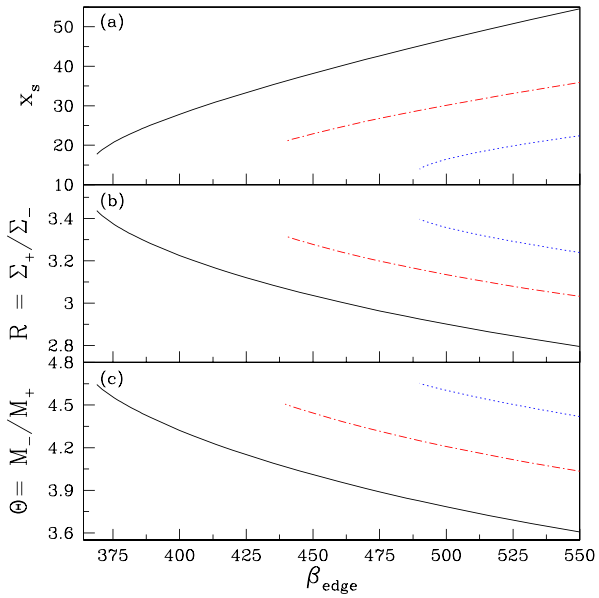

Figure 7. Variation of different flow properties such as (a) the shock location x_s, (b) shock compression ratio R, and (c) shock strength Θ as a function of β_{edge} for different values of λ_{edge}. Flows is injected from $x_{edge} = 1000$ with $\mathcal{E}_{edge} = 1.9133 \times 10^{-4}$, $\alpha_B = 0.01$ and $\xi = 20$, respectively. Results represented by the solid curve is for $\lambda_{edge} = 1.892$ and the dot–dashed and dotted curves are for $\lambda_{edge} = 1.874$ and 1.856. See text for details.

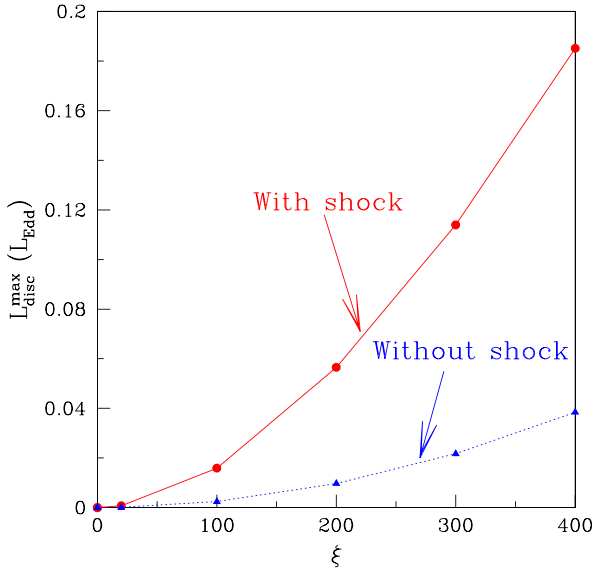

Figure 8. Variation of maximum disc luminosity L_{disc}^{max} as a function of cooling efficiency factor ξ. Filled circles connected with solid line and filled triangles connected with dotted line are for shocked and shock free accretion solutions.

that the centrifugal force seems to play a crucial role in deciding the possibility of shock formation.

As discussed in Section 2 that the bremsstrahlung emissivity directly depends on the density and temperature of the flow and therefore, the emergent radiations from the disc are also depend on them. Hence, it is useful to calculate the density and temperature distributions of the flow across the shock discontinuity as both the density and temperature are enhanced due to shock compression in the post-shock flow. For that, first we calculate the compression ratio that determines the density compression of the flow across the shock and is defined as the ratio of the vertically averaged post-shock density to the pre-shock density ($R = \Sigma_+/\Sigma_-$). In Fig. 6(b), we plot the variation of compression ratio as function of cooling efficiency factor for the same set of input parameters as in Fig. 6(a). A positive correlation is observed in all cases as the compression ratio is increased with the increase of cooling rate. This is quite natural because higher cooling efficiency pushes the shock front inward that causes more compression in the post-shock flow and eventually, compression ratio increases. When the cooling efficiency factor is reached its critical value, we observe a cut-off in the variation of compression ratio. This happens in all cases as the standing shock fails to exist there. Further, we calculate the shock strength (Θ) which is defined as the ratio of pre-shock Mach number (M_-) to the post-shock Mach number (M_+) and it measures the temperature jump across the shock. In Fig. 6(c), we plot shock strength as function of ξ for the same set of input parameters as in Fig. 6(a) and observe the variation of Θ very similar to R as depicted in Fig. 6(b).

We continue our study to investigate the shock properties in terms of β_{edge} for flows with same outer boundary values, namely, $x_{edge} = 1000$, $\mathcal{E}_{edge} = 1.9133 \times 10^{-4}$, $\alpha_B = 0.01$ and $\xi = 20$. In Fig. 7, the solid, dot–dashed and dotted curves are for $\lambda_{edge} = 1.892$, 1.874 and 1.856, respectively. As discussed in Fig. 5, here also the shock location is reduced with the decrease of β_{edge} for all cases having different angular momentum at the outer edge. Interestingly, the lower limit of β_{edge} is not indefinite, because the possibility of shock transition ceases to exist when β_{edge} is reduced to its critical limit. With this, we compute the shock compression ratio (R) and the shock strength (Θ) as in Figs 6(b and c) and find that both are increased when β_{edge} is decreased gradually.

3.4 Accretion disc luminosity

In this work, we consider the Bremsstrahlung emission process as the prospective cooling mechanism for flows accreting on to black holes. Following this, we estimate the disc luminosity (L_{disc}) as

$$L_{disc} = 4\pi \int_{x_{in}}^{x_{edge}} Q^- x \mathrm{d}x,$$

where, x_{in} and x_{edge} denote the inner sonic point and the outer edge of the disc, respectively, and Q^- is the Bremsstrahlung cooling rate. Here, we neglect radiations emitted from the region between the horizon and the inner sonic point as they are expected to be redshifted and do not contribute significantly in the disc luminosity. In Fig. 8, we present the variation of maximum Bremsstrahlung luminosity as function of cooling efficiency factor (ξ). Filled circles connected with solid lines denote the results obtained from the shock induced global accretion solution whereas the filled triangles joined with dotted lines represent the results for shock free accretion solutions. For a given cooling efficiency factor, we compute the maximum disc luminosity employing our model for shock and shock free cases. In general, we observe that the total luminosity is enhanced when ξ is increased. This is because the rise of ξ essentially increase the density of the flow and consequently flow cools efficiently. In addition, we find that for a given ξ, the disc luminosity is always higher for flows containing shock waves compared to the flows having no shocks. This apparently provides an indication that the shocked accretion solutions are perhaps potentially more preferred to study the energetics of the black hole sources.

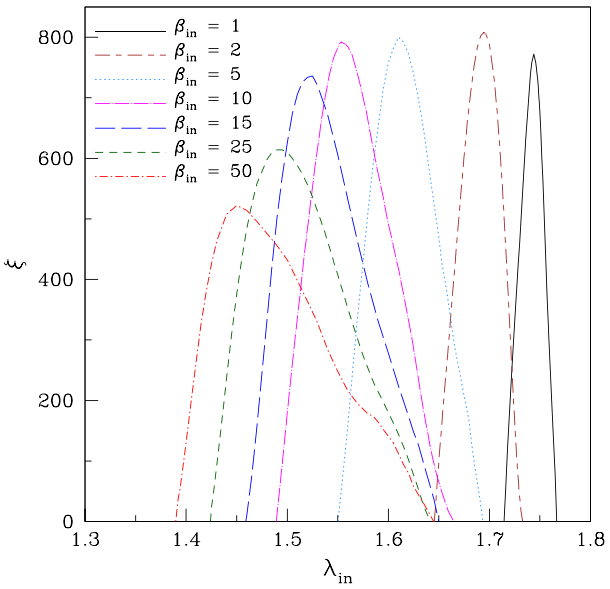

Figure 9. Separations of the parameter space that allow stationary shock waves in the $\lambda_{in} - \xi$ plane. Dot–dashed, dashed, long-dashed, dot–long dashed, dotted, short–long dashed and solid curves are for $\beta_{in} = 50$, 25, 15, 10, 5, 2 and 1, respectively. Here, we fix $\alpha_B = 0.01$. See text for details.

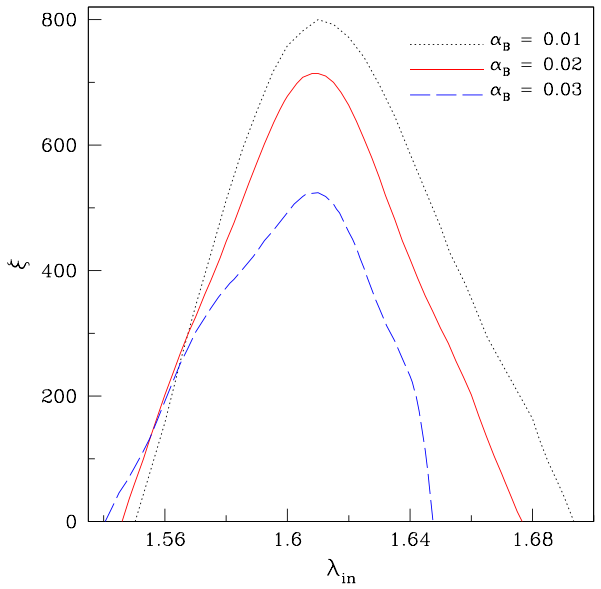

Figure 10. Effective regions of the parameter space for stationary shock in the $\lambda_{in} - \xi$ plane. The regions separated by dotted, solid and dashed curves are for $\alpha_B = 0.01$, 0.02 and 0.03, respectively. Here, we fix $\beta_{in} = 5$. See text for details.

3.5 Parameter space for shock

It is already pointed out that the dissipative global accretion solutions including shock waves are not the isolated solutions, instead such solutions exist for a wide range of angular momentum and the cooling efficiency factor. In order to understand the influence of magnetic field on the properties of the stationary shock waves in a dissipative accretion flow, we identify the region of the parameter space spanned by the angular momentum at the inner sonic point (λ_{in}) and the cooling efficiency factor (ξ) that provides shock solutions and subsequently classify them in terms of β_{in}. Here, β_{in} refers to the value of β measured at the inner sonic point x_{in}. The results are depicted in Fig. 9 where, we choose $\alpha_B = 0.01$. The dot–dashed boundary separates the shock parameter space and is obtained for $\beta_{in} = 50$ where magnetic pressure is weak and accretion flow is tended to be gas pressure dominated. As the strength of the magnetic pressure is increased relative to the gas pressure, the parameter space shifts towards the higher angular momentum side. This is due to the fact that the range of angular momentum at the inner sonic point for transonic accretion flow increases when β_{in} is decreased. Here, dashed, long-dashed, dot–long dashed, dotted, short–long dashed and solid curves identify the boundary for $\beta_{in} = 25$, 15, 10, 5 2 and 1, respectively. We observe that when the accretion flow starts dominated by the magnetic pressure, the effective region of the parameter space for standing shocks reduces gradually and finally disappears when β_{in} reached its critical value.

We continue our study of parameter space to explore the role of viscous dissipation in the shock parameter space. While doing so, we choose $\beta_{in} = 5$ all throughout and obtain the parameter space as function of α_B which is depicted in Fig. 10. As before, here again we find that shock induced global accretion solutions can be obtained for a wide range of input parameters, namely λ_{in} and ξ. In the figure, the viscous dissipation parameters are marked. We observe that as the dissipation is increased, the parameter space for stationary shock is shrunk. This is simply because the possibility of shock transition is reduced with the enhancement of dissipation in the flow. Eventually, the shock parameter space disappears when α_B is crossed its critical value.

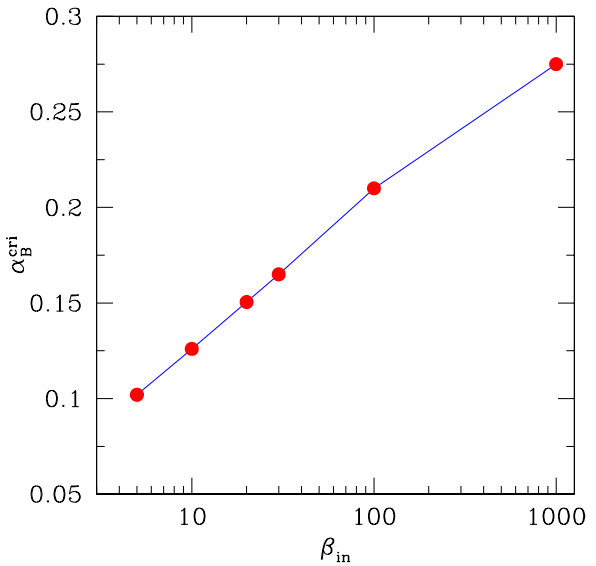

Figure 11. Variation of critical viscosity parameter (α_B^{cri}) with β_{in} that allows standing shocks. Here, we consider $\xi = 20$. See text for details.

3.6 Critical viscosity parameter

In the previous section, we have pointed out that the dynamical structure of the global accretion flow changes when the viscosity parameter exceeds its critical value. Following this, we obtain the value of the critical viscosity parameter α_B^{cri} based on the criteria of whether a standing shock is formed or not. Evidently, the critical viscosity parameter largely depends on the inflow parameters. In Fig. 11, we demonstrate the variation of α_B^{cri} with β_{in} for $\xi = 20$. In a magnetized flow, the angular momentum transport in the disc equatorial plane is increased as the magnetic pressure contributes

Table 1. Estimation of shock luminosity. Column 1 lists the names of the sources and columns 2 and 3 give mass and accretion rate. Columns 4–7 provide the model parameters and columns 8–10 denote the maximum energy dissipation, shock location and estimated maximum shock luminosity obtained from equation (20). Observed core radio luminosity values are given in column 11.

Object	$M_{\rm BH}$ ($M_\odot$)	$\dot{m}$ ($\dot{M}_{\rm Edd}$)	$\mathcal{E}_{\rm out}$ ($10^{-4}c^2$)	$\lambda_{\rm out}$ ($cr_{\rm g}$)	$\beta_{\rm out}$	$\Delta\mathcal{E}'$	$\Delta\mathcal{E}^{\rm max}$ ($10^{-3}c^2$)	x_s ($r_{\rm g}$)	$L_{\rm shock}^{\rm max}$ (erg s^{-1})	$L_{\rm jet}^{\rm Obs}$ (erg s^{-1})
Sgr A*	4.90×10^{6}[a]	2.776×10^{-4}[b]	2.356	1.643	1000	0.65	3.637	13.66	6.2×10^{38}	1.0×10^{39}[c]
NGC 4258	3.39×10^{7}[d]	9.423×10^{-5}[e]	1.996	1.637	3500	0.71	3.937	14.48	1.6×10^{39}	1.0×10^{42}[c]
NGC 3079	6.76×10^{7}[d]	5.907×10^{-3}[e]	2.129	1.630	2400	0.64	3.835	13.42	1.9×10^{41}	4.0×10^{41}[f]
Mrk 79	5.24×10^{7}[g]	1.125×10^{-2}[h]	2.219	1.635	2000	0.74	4.242	13.39	3.1×10^{41}	3.4×10^{40}[h]
NGC 6500	1.70×10^{8}[d]	8.000×10^{-6}[i]	2.125	1.633	3000	0.70	4.089	13.51	6.9×10^{38}	7.9×10^{38}[j]
M87	3.50×10^{9}[k]	1.192×10^{-4}[l]	2.468	1.669	330	0.34	1.938	13.72	1.0×10^{41}	5.0×10^{44}[m]

References: [a]Aschenbach et al. (2010), [b]Yuan, Markoff & Falcke (2002), [c]Falcke & Biermann (1999), [d]Kadowaki, de Gouveia Dal Pino & Singh (2015), [e]Yamauchi et al. (2004), [f]Shafi et al. (2015), [g]Peterson et al. (2004), [h]Riffel, Storchi-Bergmann & Winge (2013), [i]Satyapal, Sambruna & Dudik (2004), [j]Falcke, Kording* & Markoff (2004), [k]Walsh et al. (2013), [l]Kuo et al. (2014), [m]de Gasperin et al. (2012).

to the total pressure. Hence, a lower value of α_B is sufficient to transport angular momentum required for shock formation. On the contrary, the possibility of shock formation is enhanced with the higher viscosity parameter when the flow is shifted towards the gas pressure dominated regime. As $\beta_{\rm in}$ is increased, the critical viscosity parameter $\alpha_B^{\rm cri}$ tends to approach $\alpha_\Pi^{\rm cri}$ ($\sim$0.3) as estimated by the Chakrabarti & Das (2004) for gas pressure dominated flow.

4 ASTROPHYSICAL APPLICATIONS

So far, we have concentrated on the accretion shocks around black holes where the specific energy across the shock front is considered to be constant (Chakrabarti 1989) and these shocks are radiatively inefficient in nature. However, in reality, the characteristic of the shocks can be dissipative as well where a part of the accreting energy is released vertically through the disc surface at the shock location causing the reduction of specific energy in the PSC (Singh & Chakrabarti 2011). Usually the energy dissipation mechanism at the shock is regulated by the thermal Comptonization process (Chakrabarti & Titarchuk 1995) and therefore, the thermal distribution in the PSC is reduced. Based on this criteria, we estimate the energy loss across the shock where we assume that the loss of energy is scaled with the temperature difference between the immediate post-shock and pre-shock flow and is given by (Das, Chakrabarti & Mondal 2010)

$$\Delta\mathcal{E} = \Delta\mathcal{E}'(a_+^2 - a_-^2), \tag{19}$$

where, a_+ and a_- are the post-shock and pre-shock sound speeds, respectively, and $\Delta\mathcal{E}'$ denotes the fraction of the thermal energy difference lost in this process which we treat as a parameter. For a weakly rotating black hole, Das et al., 2010 calculated the maximum energy dissipation at the shock and is estimated as $\Delta\mathcal{E}^{\rm max} \sim 2.5$ per cent. Needless to mentioned that $\Delta\mathcal{E}$ chosen beyond this range does not provide global transonic accretion solution including shock waves.

In this scenario, the accessible energy at the PSC is same as the available energy dissipated at the shock. A fraction of this energy is converted in to high-energy radiations and the remaining part of the energy is utilized to produce jets as they are likely to originate from the PSC around the black holes. Subsequently, these jets simultaneously ingest a part of this energy for the work done against gravity and for carrying out their thermodynamical expansion. The remaining part of the energy is then utilized to power the jets. Therefore, according to the energy budget, the total usable energy available in the post-shock flow is $\Delta\mathcal{E}$ and the corresponding loss of kinetic power from the disc can be estimated in terms of the observable quantities as in Le & Becker (2004, 2005)

$$L_{\rm total} = L_{\rm shock} = \dot{M} \times \Delta\mathcal{E} \times c^2 \ \ {\rm erg\ s^{-1}}, \tag{20}$$

where, $L_{\rm total}$ is the kinetic power lost by the disc, $L_{\rm shock}$ is the shock luminosity and $\dot{M}$ is the accretion rate for a given source, respectively. Following the above approach, we estimate the maximum shock luminosity ($L_{\rm shock}^{\rm max}$) that corresponds to maximum energy dissipation at the shock. Here, $\alpha_B = 0.001$ and $\xi = 10$ are considered for all cases. In Table 1, we present the physical parameters of the supermassive black hole sources including model parameters and estimated maximum shock luminosity. In columns 1–3, we display the list of sources, their mass ($M_{\rm BH}$) and dimensionless accretion rate ($\dot{m}$). In columns 4–6, we indicate the representative values of flow variables at the outer sonic point, namely energy $\mathcal{E}_{\rm out}$, angular momentum $\lambda_{\rm out}$ and $\beta_{\rm out}$. In column 7, we mention the $\Delta\mathcal{E}'$ value that provides the maximum $\Delta\mathcal{E}^{\rm max}$ (in column 8) and shock location x_s (in column 9). In column 10, we present the maximum shock luminosity $L_{\rm shock}^{\rm max}$. In this analysis, our motivation is to quantify the upper limit of the energy that can be extracted from the PSC to power the deflected matter from the disc as Jets. Therefore, we calculate the maximum energy dissipation $\Delta\mathcal{E}^{\rm max}$ at the location of shock transition. We find that the estimated shock luminosities for supermassive black hole sources under consideration are in close agreement with the observed core radio luminosity values $L_{\rm jet}^{\rm Obs}$ (in column 11) (Falcke & Biermann 1999; Falcke et al. 2004; de Gasperin et al. 2012; Riffel et al. 2013; Shafi et al. 2015).

5 CONCLUSIONS

In this paper, we have studied the dynamical structure of a magnetized accretion flow around a non-rotating black hole in presence of Bremsstrahlung cooling. Since the exact physical mechanism for angular momentum transport in an accretion disc is not yet conclusive, we assume that the Maxwell stress is proportional to the total pressure following the work of Machida et al. (2006), where the constant of proportionality α_B plays the role similar to the conventional viscosity parameter as described in Shakura & Sunyaev (1973). We indeed find that such an accretion flow is transonic in nature. This is because the inflowing matter must satisfy the inner boundary condition imposed by the black hole horizon. Depending on the flow parameters, namely angular momentum (λ), viscosity (α_B), cooling efficiency factor (ξ) and β, respectively, accreting matter changes its sonic state multiple times as it contains multiple sonic points. Flows of this kind are of special interest as they may contain shock wave which is perhaps essential to understand the spectral and timing

properties of the black hole candidates (Chakrabarti & Manickam 2000; Nandi et al. 2001a,b, 2012; Radhika & Nandi 2014; Iyer et al. 2015).

In Section 3, we calculate the shock induced global accretion solution in presence of toroidal magnetic field. Due to shock transition, the post-shock flow, e.g. PSC is compressed and as a consequence PSC becomes hot and dense as is seen in Fig. 3. According to our solutions, PSC remains optically thin though there is a sharp rise of density at the inner part of the disc. This effectively enhances the possibility of escaping the hard radiations from PSC. When the cooling efficiency is increased, the thermal pressure of PSC is evidently reduced. As a consequence, shock front moves towards the horizon and finally settles down at a smaller radius where total pressure across the shock front is balanced. Above the critical cooling limit ($\xi^{\rm cri}$), PSC disappears due to effect of excess cooling where shock conditions are not favourable. It must be noted that $\xi^{\rm cri}$ does not correspond to a unique value as it depends of the other flow parameters.

One of the important results of this work is to obtain the global shock solutions in gas pressure dominated flow as well as magnetic pressure dominated flow and subsequently investigate the dependences of flow parameters on shock properties. In Figs 6 and 7, we observe that global shock solutions are not the isolated solutions, instead shock may form for a wide range of flow parameters. Moreover, we find that α_B and β play important role in deciding the formation of shock waves (Figs 9 and 10).

We also calculate the critical viscosity parameter ($\alpha_B^{\rm cri}$) that allows standing shocks in the accretion flow around black holes. Beyond this critical limit, standing shock conditions are not favourable and hence, steady shock ceases to exist. We find that $\alpha_B^{\rm cri}$ gradually increases as the plasma β increases and ultimately tends to the value $\sim$0.3 as reported by Chakrabarti & Das (2004) for gas pressure dominated flow (Fig. 11). For $\alpha_B > \alpha_B^{\rm cri}$, however, oscillatory shocks may still form (Das et al. 2014) which is the next issue to be undertaken and will be reported elsewhere.

Further, we self-consistently study the characteristics of the dissipative shock solutions. In this scenario, a part of the accreting energy is escaped from the shock location in the vertical directions through the disc surface and this dissipated energy is being utilized to power the jets (Chakrabarti & Titarchuk 1995; Le & Becker 2004, 2005). In order to understand the implications of the dissipative shock, we estimate the maximum shock luminosity ($L_{\rm shock}^{\rm max}$) corresponding to the maximum energy dissipation ($\Delta\mathcal{E}^{\rm max}$) at the shock using equations (19) and (20). In Table 1, we summarize the physical parameters of the black hole sources along with the model parameters and $L_{\rm shock}^{\rm max}$. We observe that the estimated $L_{\rm shock}^{\rm max}$ for several supermassive black hole sources are in close agreement with the observed core radio luminosity values ($L_{\rm jet}^{\rm Obj}$).

Finally, we point out that the present formalism is developed based on some approximations. We ignore the rotation of the black hole and use pseudo-Newtonian potential to describe the space–time geometry around a non-rotating black hole as it allows us to study the non-linear shock solutions in a simpler way. We neglect the synchrotron emission process in this work although it is expected to play an role in a magnetized accretion flow. An extension of our present study including synchrotron cooling to the case of rotating black hole is under progress and will be reported elsewhere. Also, the adiabatic index of the flow is considered to be a global constant instead of calculating it self-consistently using thermal properties of the flow. Of course, the implementation of such issue is beyond the scope of this paper, however, we believe that the basic conclusions of this work will remain qualitatively unaltered.

ACKNOWLEDGEMENTS

Authors would like to thank Anuj Nandi for discussions. Authors also thank the anonymous referee for useful comments and constructive suggestions.

REFERENCES

Akizuki C., Fukue J., 2006, PASJ, 58, 469
Aktar R., Das S., Nandi A., 2015, MNRAS, 453, 3414
Aschenbach B., 2010, Mem. Soc. Astron. Ital., 81, 319
Balbus S., Hawley J. F., 1991, ApJ, 376, 214
Balbus S., Hawley J. F., 1998, Rev. Mod. Phys., 70, 1
Becker P. A., Kazanas D., 2001, ApJ, 546, 429
Le T.Becker P. A., Das S., 2008, ApJ, 677, L93
Begelman M. C., Pringle J. E., 2007, MNRAS, 375, 1070
Bu D.-F., Yuan F., Xie F.-G., 2009, MNRAS, 392, 325
Chakrabarti S. K., 1989, ApJ, 347, 365
Chakrabarti S. K., 1990, Theory of Transonic Astrophysical Flows. World Scientific, Singapore
Chakrabarti S. K., 1996, ApJ, 464, 664
Chakrabarti S. K., 1999, A&A, 351, 185
Chakrabarti S. K., Das S., 2004, MNRAS, 349, 649
Chakrabarti S. K., Manickam S. G., 2000, ApJ, 531, L41
Chakrabarti S. K., Titarchuk L., 1995, ApJ, 455, 623
Chattopadhyay I., Chakrabarti S. K., 2000, Int. J. Mod. Phys. D, 9, 717
Chattopadhyay I., Chakrabarti S. K., 2002, MNRAS, 333, 454
Chattopadhyay I., Das S., 2007, New Astron., 12, 454
Das S., 2007, MNRAS, 376, 1659
Das S., Chakrabarti S. K., 2004, Int. J. Mod. Phys. D, 13, 1955
Das S., Chattopadhyay I., 2008, New Atsron., 13, 549
Das S., Chattopadhyay I., Nandi A., Chakrabarti S. K., 2001a, A&A, 379, 683
Das S., Chattopadhyay I., Chakrabarti S. K., 2001b, ApJ, 557, 983
Das S., Becker P. A., Le T., 2009, ApJ, 702, 649
Das S., Chakrabarti S. K., Mondal S., 2010, MNRAS, 401, 2053
Das S., Chattopadhyay I., Nandi A., Molteni D., 2014, MNRAS, 442, 251
de Gasperin F. et al., 2012, A&A, 547, 56
Falcke H., Biermann P. L., 1999, A&A, 342, 49
Falcke H., Kording E., Markoff S., 2004, A&A, 414, 895
Fukue J., 1987, PASJ, 39, 309
Gierliński M., Newton J., 2006, MNRAS, 370, 837
Gu W. M., Lu J. F., 2004, Chin. Phys. Lett., 21, 2551
Hirose S., Krolik L. H., Stone J. M., 2006, ApJ, 640, 901
Iyer N., Nandi A., Mandal S., 2015, ApJ, 807, 108
Kadowaki L. H. S., de Gouveia Dal Pino E. M., Singh C. B., 2015, ApJ, 802, 113
Kuo C. Y. et al., 2014, ApJ, 783, 33
Landau L. D., Lifshitz E. D., 1959, Fluid Mechanics. Pergamon, New York
Le T., Becker P. A., 2004, ApJ, 617, L25
Le T., Becker P. A., 2005, ApJ, 632, L476
Lu J. F., Gu W. M., Yuan F., 1999, ApJ, 523, 340
Machida M., Nakamura K. E., Matsumoto R., 2006, PASJ, 58, 193.
Matsumoto R., Kato S., Fukue J., Okazaki A. T., 1984, PASJ, 36, 71
Molteni D., Lanzafame G., Chakrabarti S. K., 1994, ApJ, 425, 161
Molteni D., Ryu D., Chakrabarti S. K., 1996, ApJ, 470, 460
Nagakura H., Yamada S., 2009, ApJ, 696, 2026
Nandi A., Manickam S. G., Rao A. R., Chakrabarti S. K., 2001a, MNRAS, 324, 267
Nandi A., Chakrabarti S. K., Vadawale S. V., Rao A. R., 2001b, A&A, 380, 245
Nandi A., Debnath D., Mandal S., Chakrabarti S. K., 2012, A&A, 542, 56
Narayan R., Kato S., Honma F., 1997, ApJ, 476, 49.

Oda H., Machida M., Nakamura K. E., Matsumoto R., 2007, PASJ, 59, 457
Oda H., Machida M., Nakamura K. E., Matsumoto R., 2010, ApJ, 712, 639
Oda H., Machida M., Nakamura K. E., Matsumoto R., Narayan R., 2012, PASJ, 64, 15
Okuda T., 2014, MNRAS, 441, 2354
Okuda T., Das S., 2015, MNRAS, 453, 147
Paczyński B., Wiita P. J., 1980, A&A, 88, 23.
Peterson B. M. et al., 2004, ApJ, 613, 682
Radhika D., Nandi A., 2014, Adv. Space Res., 54, 1678
Riffel R. A., Storchi-Bergmann T., Winge C., 2013, MNRAS, 430, 2249
Samadi M., Abbassi S., Khajavi M., 2014, MNRAS, 437, 3124
Satyapal S., Sambruna R. M., Dudik R. P., 2004, A&A, 414, 825
Shafi N., Oosterloo T. A., Morganti R., Colafrancesco S., Booth R., 2015, MNRAS, 454, 1404
Shakura N. I., Sunyaev R. A., 1973, A&A, 24, 337.
Shapiro S. L., Teukolsky S. A., 1983, Black Holes, White Dwarfs and Neutron Stars: The Physics of Compact Objects. Wiley-Interscience, New York.
Singh C. B., Chakrabarti S. K., 2011, MNRAS, 410, 2414
Suková P., Janiuk A., 2015, MNRAS, 447, 1565
Walsh J. L., Barth A. J., Ho L. C., Sarzi M., 2013, ApJ, 770, 86
Yamauchi A., Nakai N., Sato N., Diamond P., 2004, PASJ, 56, 605
Yuan F., Markoff S., Falcke H., 2002, A&A, 383, 854

This paper has been typeset from a TEX/LATEX file prepared by the author.